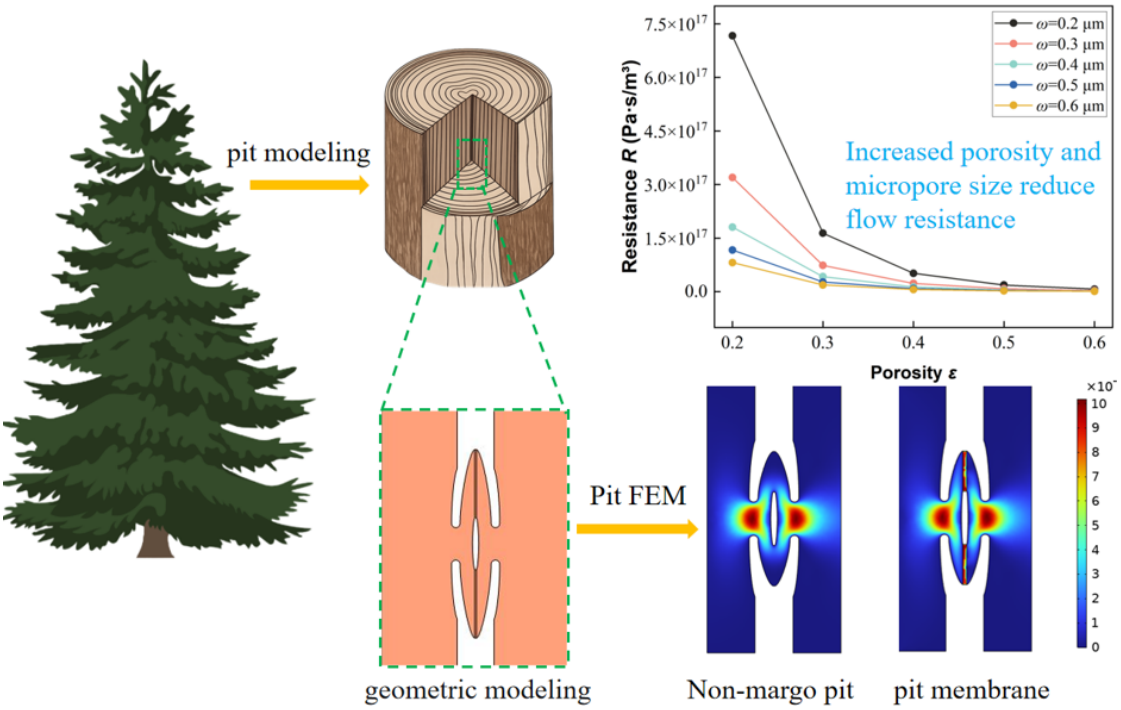
Insights into the Effect of Bordered Pit Structure on Water Transport Performance

Yifan Zhou, Tong Su, and Gensheng Wu *

*Corresponding author: genshengwu@126.com

DOI: 10.15376/biores.21.3.5984-5998

GRAPHICAL ABSTRACT



Insights into the Effect of Bordered Pit Structure on Water Transport Performance

Yifan Zhou, Tong Su, and Gensheng Wu *

In plants, the transport of water is mediated by vessel and pit structures, which are integral to this physiological process. Among the various pit types, the bordered pit is recognized as particularly effective. To investigate the impact of structural parameters on fluid flow performance, a microstructural fluid dynamics model of plant tissue was developed employing finite element simulation. This model integrates laminar flow and porous media physics within a unified framework, and the computed results agreed with existing experimental and numerical studies. An analysis was conducted to assess variations in pressure drop, flow rate, and flow resistance as a function of several parameters, including pit aperture diameter, torus diameter, pit diameter, pit depth, margo thickness, porosity, and micropore diameter. The results demonstrate that overall flow resistance decreases with increases in pit diameter, pit aperture diameter, pit depth, porosity, and micropore diameter, whereas it increases with larger torus diameter and margo thickness. Notably, parameters associated with the margo exert a particularly pronounced effect on water transport characteristics. This study provides a mechanical rationale elucidating the structure-function relationship governing water transport in coniferous plants and offers theoretical foundations for the design of biomimetic microfluidic devices and plant-inspired water-conducting materials.

DOI: 10.15376/biores.21.3.5984-5998

Keywords: Pit membrane; Torus-margo pits; Bordered pit; Computational fluid dynamics

*Contact information: College of Mechanical and Electronic Engineering, Nanjing Forestry University, Nanjing 210037, China; *Corresponding author: genshengwu@126.com*

INTRODUCTION

The hierarchical microporous structure of wood materials exhibits unique advantages in various engineering and applied contexts. Due to their natural gradient pore-size distribution, wood-based materials can function as efficient filtration and separation media, and they have been widely employed in fields such as wastewater treatment and oil-water separation (Cheng *et al.* 2020). Pits are minute pores located in the walls of water-conducting cells, such as tracheids and vessels, within the xylem tissue of wood. These structures connect adjacent cells, facilitating the intercellular movement of water, and play a critical role in either promoting or impeding the propagation of air embolisms. Among the various types of pits, bordered pits are particularly noteworthy due to their complex architecture and essential regulatory functions, which are fundamental to water transport and embolism resistance in coniferous species. The structural configuration of bordered pits directly affects a tree's hydraulic efficiency and its capacity to withstand embolism formation. Elucidating the quantitative relationship between pit morphology and flow resistance is crucial not only for understanding the mechanisms of water conduction in

trees but also for informing theoretical frameworks aimed at breeding stress-tolerant tree varieties, modifying wood properties, and modeling ecohydrological dynamics. The defining characteristics of pits manifest at micro- to nanoscale dimensions and exhibit intricate geometries that are closely associated with the orientation of wood microfibers, thus rendering them challenging to investigate using conventional optical microscopy. Although scanning electron microscopy (SEM) and transmission electron microscopy (TEM) provide higher-resolution imaging capabilities, these techniques generally necessitate sample dehydration or fixation, thereby restricting observations of pits in their native hydrated, living, or mechanically dynamic states. This limitation poses a significant obstacle to advancing comprehensive research on the mechanisms governing water transport through wood pits (Parent *et al*. 2018; Qu *et al.* 2021).

To overcome the limitations associated with experimental characterization, particularly in controlling experimental conditions, numerical simulation techniques have seen rapid advancements in recent years concerning the study of water transport functions in pits. Schulte (2011) developed a computational model of pit structures based on actual scanning electron microscopy images of spruce, preserving the real geometric features of the pits, thereby validating the applicability of numerical simulation methods in pit research and elucidating functional differences among specific pit configurations. Similarly, Qu *et al.* (2021) conducted simulations to analyze the influence of structural parameters, including torus diameter and margo thickness, on flow velocity distribution and pressure drop while maintaining authentic geometric dimensions. Their findings identified the margo as the principal structural component governing flow resistance within pits.

Despite these significant strides in numerical simulation studies of water transport in bordered pits, further refinement is necessary in both model construction and the representation of underlying physical processes. From a modeling standpoint, existing studies frequently approximate the pit membrane as a rigid solid obstacle embedded within the free fluid domain (Qu *et al.* 2021). Consequently, the theoretical frameworks employed predominantly rely on the Navier-Stokes (N-S) equations (Schulte 2011; Li *et al.* 2020), without adequately incorporating porous media dynamics. This simplification compromises the accuracy of flow behavior representation within the inherently porous margo structure, thereby limiting the capacity to capture permeation and retention phenomena characteristic of the pit membrane as a porous medium.

Addressing these challenges, Ruan and Rybak (2025, 2026) introduced a mixed-dimensional Stokes-Brinkman-Darcy (SBD) theoretical framework, which offers a more realistic and robust modeling approach for simulating water transport in bordered pits. The central innovation of the SBD theory is the introduction of a transitional zone bridging the laminar flow region and the porous medium, wherein the averaged Brinkman equation is applied to model fluid flow, accounting for viscous shear forces, while the convective inertial terms are negligible due to the low Reynolds number regime. This approach enables adaptability to arbitrary flow directions. The SBD theory has demonstrated high suitability for problems involving the coexistence of free flow and micro-porous media. Moreover, it substantially reduces the computational burden associated with fully resolving intricate real geometries while maintaining physical fidelity, thereby facilitating more efficient numerical solutions and providing an effective theoretical tool for optimizing simulation methodologies.

To address the prevalent deficiency of porous media simulation in existing investigations of water transport within pits, this study develops a multiphysics model of bordered pits grounded in the SBD theory. Employing the finite element method, the fluid

dynamic behavior associated with water transport is simulated. Furthermore, quantitative analyses are conducted to elucidate the relationships between critical structural parameters, including the pit and margo, and flow resistance. Additionally, the effects of micropore size and porosity on the margo surface on water flow characteristics within pits are systematically examined.

EXPERIMENTAL

Model Development

Pits are mainly composed of the pit chamber and pit membrane. Based on whether the cell wall around the pore opening is raised to form a pit border, pits can be classified into bordered pits and simple pits. In the study by Schulte (2011), the radial section of wood was obtained by axial splitting, and high-resolution images of pits on this surface were captured using SEM, thereby establishing a pit model that reflects the real geometric structure. Therefore, this study refers to this geometrically accurate model based on the radial section and simulates fluid transport within pits by finite element method (FEM). As depicted in Fig. 1, the principal components of a bordered pit include the pit aperture, pit border, torus, and margo. The torus, which is relatively thick, can be regarded as an impermeable structure, whereas the margo is a membranous structure characterized by numerous micropores distributed across its surface. Fluid flow within woody materials is generally considered laminar due to the low Reynolds number. However, as shown in the structural diagram of the bordered pit in Fig. 1, the pit border generates transition zones on both sides of the pit chamber where curvature varies sharply. This geometric feature can induce sudden changes in flow velocity and pressure as incompressible fluid passes through the pit aperture (Li *et al.* 2020). Furthermore, when fluid traverses the porous margo surface, it is partitioned into multiple fine streams by the micropores, which may give rise to localized turbulence. Consequently, employing a single Navier-Stokes (N-S) equation to characterize the entire fluid flow within bordered pits is inadequate. Instead, the model should be segmented into two distinct regions—the inlet/outlet and the pit chamber—with appropriate fluid dynamic equations applied independently to each region.

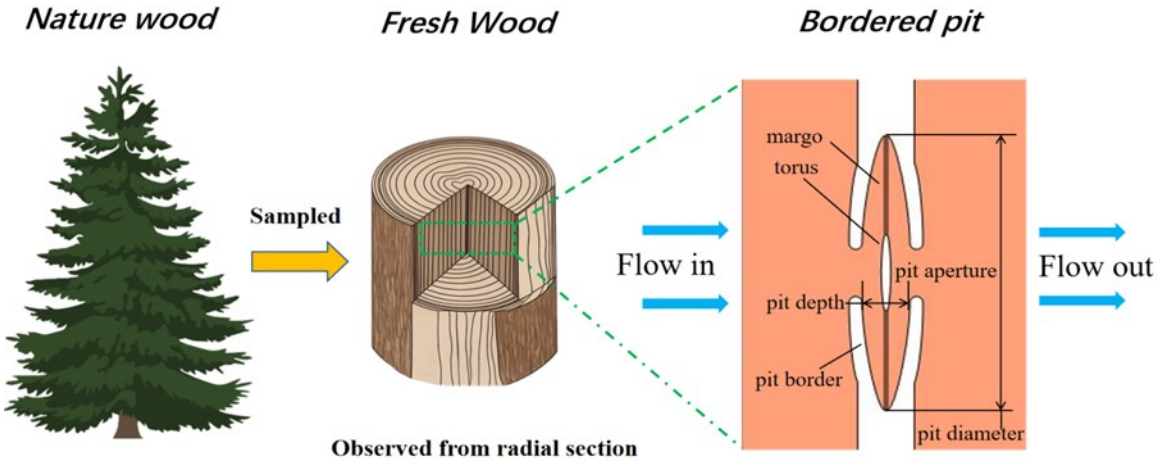


Fig. 1. Diagram of a bordered pit structure

Conventional fluid dynamics frameworks commonly utilize the Navier-Stokes (N-S) equations to characterize laminar flow and Darcy's law to represent flow within porous media. Nonetheless, this mechanical coupling of physical domains is generally constrained to scenarios where the flow direction is straightforward and aligned parallel to the interface. Expanding on this approach, the SBD theory incorporates the Brinkman equation to model the transitional region between the laminar flow domain and the porous media domain, thereby providing a more accurate representation of water transport in bordered pits. The inlet and outlet regions of pits exemplify typical laminar flow zones; consequently, the behavior of an incompressible fluid within these areas is described by the N-S equations,

$$\nabla \cdot \vec{u} = 0 \tag{1}$$

$$\rho\left(\frac{\partial \vec{u}}{\partial t} + \left(\vec{u} \cdot \nabla\right)\vec{u}\right) = -\nabla p + \mu \nabla^2 \vec{u} \tag{2}$$

where $\vec{u}$ denotes the fluid velocity in m/s, ρ denotes the fluid density in kg/m³, p denotes the pressure in Pa, μ denotes the dynamic viscosity in Pa·s, and g denotes the gravitational acceleration. Equation 1 represents the continuity equation describing fluid motion within the pit, while Eq. 2 represents the momentum equation.

Due to the low Reynolds number regime in this study, the convective inertial terms in the governing equations are negligible and have been omitted. The torus-margo complex in the pit chamber can be regarded as a micro-/nano-scale fibrous porous medium. After the incompressible fluid enters the inlet region of the pit, the momentum equation for the fluid in the margo region is as follows,

$$\frac{\rho}{\varepsilon}\left(\frac{\partial \vec{u}}{\partial t} + \frac{1}{\varepsilon}\left(\vec{u} \cdot \nabla\right)\vec{u}\right) = -\nabla p + \frac{\mu}{\varepsilon}\nabla^2 \vec{u} - \frac{\mu}{\mathrm{K}}\vec{u} \tag{3}$$

where ε represents the porosity, and K denotes the permeability, a parameter that characterizes the fluid's capacity to traverse the medium and is measured in square meters (m²). Equation 3 delineates the Brinkman equation integrated with Darcy's law, wherein the term $-\mu\vec{u}/\mathrm{K}$ signifies the Darcy resistance component, indicative of the volumetric flow resistance within the porous media domain. The relationship between porosity and permeability is described using the Kozeny-Carman equation:

$$\mathrm{K} = \frac{d^2\varepsilon^3}{180\left(1-\varepsilon\right)^2} \tag{4}$$

It is worth noting that employing the Brinkman equation to describe flow within the margo does not imply that the margo is being treated as a continuous porous medium satisfying the strict volume-averaging assumption in the traditional REV sense. In fact, because the geometric thickness of the margo is considerably smaller than the micropore diameter, the classical REV assumption can hardly hold rigorously in such micro/nano-scale thin-layer structures. However, as demonstrated by Lesinigo *et al*. (2010) in their study of flow in thin fractures, the advantage of the Brinkman equation lies in its ability to incorporate the collective effects of the microscopic pore structure—including both Darcy seepage resistance and Brinkman viscous shear effects—into the governing equations through macroscopic parameters such as permeability and porosity, without the need to

fully resolve each micropore geometrically. In this study, a full-dimensional geometric modeling approach is adopted (*i.e.*, directly constructing an axisymmetric model that includes the complete thickness of the margo). The Brinkman equations are solved directly on this geometry. Therefore, the present approach does not rely on the REV assumption for volume averaging. This treatment is essentially a porous medium equivalent modeling method, the validity of which has been extensively verified in fields such as groundwater hydrology and biofluid mechanics.

To facilitate a quantitative assessment of water flow through pits exhibiting varying structural dimensions, the flow resistance R was introduced as an analytical metric, complementing the conventionally employed parameters of pressure drop Δp and flow rate Q commonly utilized in related investigations. This approach follows the methodology proposed by Xia *et al.* (2024) in their examination of the bordered pits of *Platycladus orientalis*. The flow resistance encapsulates the overall obstructive effect of the pit structure on fluid flow and is mathematically defined as follows.

$$R = \frac{\Delta p}{Q} \tag{5}$$

The geometric parameters of pits analyzed in the model mainly include pit diameter D, pit aperture diameter d, torus diameter T, margo thickness t, and pit depth L. Additionally, the effects of margo surface porosity ε and micropore diameter ω on water transport behavior were examined. Based on existing studies on the bordered pits of coniferous trees such as spruce and *Platycladus orientalis*, initial dimensions were assigned to each key structural parameter in the model. The initial values were set as follows: pit diameter D is 10.00 μm; pit aperture diameter d is 1.00 μm; torus diameter T is 3.5 μm; margo thickness t is 0.05 μm; pit depth L is 1.8 μm; porosity ε is 0.44; and micropore diameter ω is 0.2 μm (Hacke and Jansen 2009; Held *et al.* 2021; Qu *et al.* 2021). In this study, the torus is treated as an impermeable solid obstacle, and the margo is modeled as a rigid porous medium with fixed geometry. This rigid-structure assumption, which is commonly adopted in computational fluid dynamics studies of bordered pits (Schulte 2011; Qu *et al*. 2021), makes it possible to isolate the purely hydraulic effects of geometric parameters without the additional complexity of fluid-structure interaction. It should be noted, however, that under elevated pressure differentials, the margo may undergo stretching in reality, which could further increase flow resistance. Therefore, the hydraulic conductivity predicted by the present model represents an upper bound under the assumption of no structural deformation.

Boundary Conditions

Previous research underscores the importance of selecting appropriate parameters for flow velocity, density, and dynamic viscosity to ensure the stability of fluid flow within porous media and to achieve convergence in numerical simulations. This consideration is particularly critical in microstructural features such as pits, where excessively high flow velocities can lead to non-physical turbulence or numerical instability. Given the characteristically slow water flow observed in natural biological porous media (Tripathi *et al.* 2025), $\vec{u}$ was prescribed as 1×10^{-4} m/s to maintain a stable laminar flow regime and to preclude the complexities associated with turbulent flow. The inlet pressure was calculated by taking the area-weighted average over the entire inlet boundary:

$$p_{in} = \frac{1}{A}\int pdA \tag{6}$$

In Eq. 6, A represents the area of the inlet boundary, while p denotes the pressure corresponding to each infinitesimal surface element on the inlet boundary. The outlet pressure was fixed at 0 Pa. All wall boundaries were modeled as smooth surfaces with a no-slip boundary condition. ρ and μ were assigned values of 999.8 kg/m³ and 1×10^{-3} Pa·s, respectively, reflecting the physical properties of pure water at ambient temperature. g was set to 9.8 m/s².

Meshing

The geometric representation of the bordered pit was discretized employing a mesh configuration, as depicted in Fig. 2. The entire model was discretized using free tetrahedral elements. Given that the inlet and outlet regions were designated as stable laminar flow zones, the mesh within these laminar flow areas was relatively coarse, as illustrated in Fig. 2(a). Conversely, the transition region of the pit chamber exhibited pronounced geometric curvature variations and complex multiphysical coupling phenomena, resulting in steep gradients in velocity and pressure (Igarashi *et al.* 1988). Additionally, the margo region, modeled as a porous medium governed by the Brinkman equation, comprises extremely fine microporous structures. Fluid flow within this domain is influenced not only by Darcy's law but also significantly affected by viscous shear forces, thereby manifesting nonlinear and multiscale characteristics in both the flow field and pressure loss (Elkady *et al.* 2022). To accurately resolve the detailed flow features and pressure losses, these regions were further refined with an exceptionally fine mesh, as shown in Fig. 2(b).

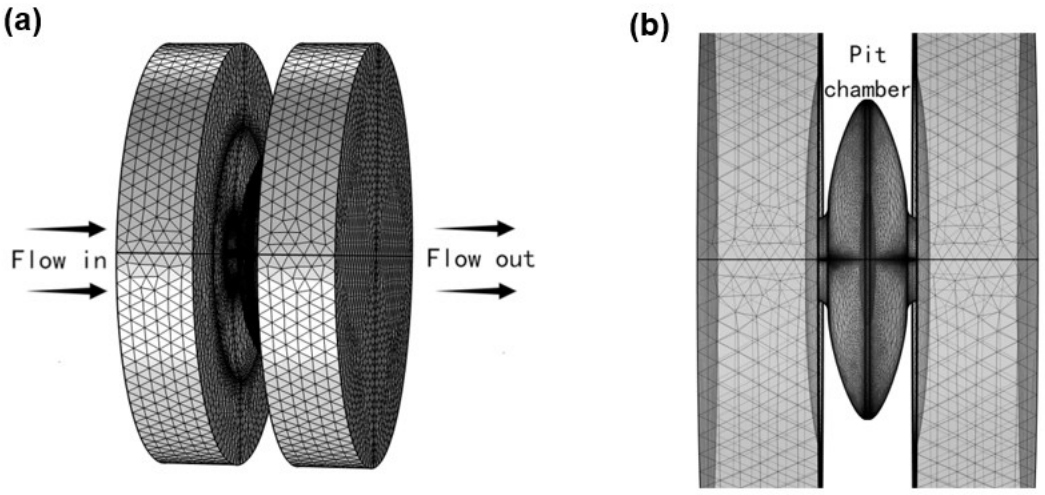


Fig. 2. Mesh distribution in the pit model

Table 1. Mesh Independence Verification

Mesh Level	Number of Elements	△p (%)
Extremely fine	921630	-
Extra fine	895075	0.38
Finer	443854	0.43
Fine	309464	1.44
Normal	243444	2.91

To verify mesh independence, a series of successively refined meshes were generated, ranging from 243,444 to 921,630 elements. The pressure drop across the pit model was computed for each mesh, and the results were compared against the values obtained from the finest mesh (Extremely fine). As shown in Table 1, the difference in pressure drop relative to the finest mesh decreases monotonically with mesh refinement, dropping from 2.91% for the Normal mesh to 0.38% for the Extra fine mesh, with the percentage difference falling below 1%. Consequently, it is inferred that the simulation results at this mesh resolution are independent of the mesh density.

RESULTS AND DISCUSSION

To elucidate the impact of the pit border–margo composite architecture on water transport dynamics within bordered pits, simulation outcomes also encompass configurations lacking either the pit membrane or the margo. The model excluding the pit membrane retains solely the inlet/outlet and pit chamber components. As illustrated in Fig. 3(a), a substantial stagnant zone emerges throughout much of the pit chamber, characterized by negligible fluid flow. This phenomenon arises from the abrupt geometric constriction and expansion, compelling the fluid to traverse the path of minimal flow resistance. The maximum velocity is observed within the central channel of the pit chamber, diminishing rapidly to zero toward the lateral boundaries. In Fig. 3(b), the introduction of an impermeable torus necessitates fluid flow circumvention of this structure upon entry through the pit aperture. The interstitial space between the torus and the pit wall facilitates broader fluid dispersion, nearly enveloping the torus. Within the complete pit model, the presence of the porous margo substantially modifies the intra-pit flow regime. As depicted in Fig. 3(c), the margo modifies the velocity distribution within the pit chamber, with higher velocities localized in regions of higher permeability, reflecting the spatially averaged effects of the microporous structure. Comparative analysis indicates that the torus-margo composite structure markedly alters fluid distribution patterns within the pit chamber. The margo emerges as the principal determinant affecting variations in flow resistance during water transport. The underlying mechanisms governing this influence will be examined in greater detail through comprehensive analysis of structural parameters.

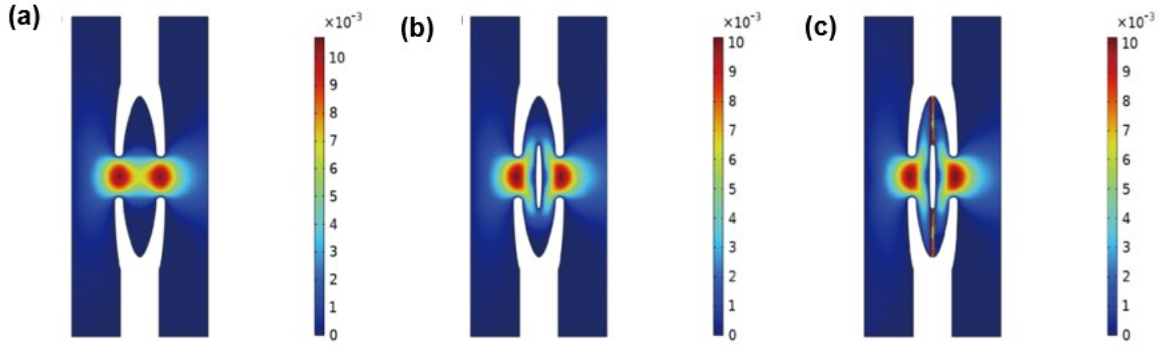


Fig. 3. Distribution of velocity field in pits, m/s (a) Non-membrane pit; (b) Non-margo pit; (c) pit membrane

Pit Aperture Diameter

Figure 4 depicts the effect of variations in pit aperture diameter on the fluid flow characteristics within pits. The data indicate that as the pit aperture diameter d increases from 1 to 5 μm, the pressure drop decreases marginally from 298.42 to 292.68 Pa. Notably, the flow rate Q remains constant at 3.35×10^{-14} m³/s regardless of changes in d. Correspondingly, the flow resistance exhibits a slight reduction, declining from 8.91×10^{15} to 8.71×10^{15} Pa·s/m³. The reliability of these computational results is supported by comparison with previous experimental and numerical studies. Lancashire and Ennos (2002) used large-scale physical models (1830-fold magnification) to measure the hydrodynamic resistance of bordered pits in *Tsuga canadensis*, reporting a single-pit resistance of 1.70×10^{15} Pa·s/m³ after scaling to real dimensions. This value is of the same order of magnitude as the presently calculated resistance, providing experimental validation for the model. Furthermore, the predicted flow rate of 3.35×10^{-14} m³/s is in excellent agreement with the lattice Boltzmann simulations of Qu *et al.* (2021), who reported 3.28×10^{-14} m³/s for a 10.23 μm pit in *Pinus sylvestris*, and aligns in magnitude with the values reported by Schulte *et al.* (2015).

These computational findings suggest that enlarging the aperture size facilitates a reduction in flow resistance during water transport through pits, attributable to the increased cross-sectional area available for flow. However, since the boundary conditions maintained a constant initial fluid velocity and a fixed pit diameter d, the Q remained unchanged, resulting in only a minimal variation in flow resistance.

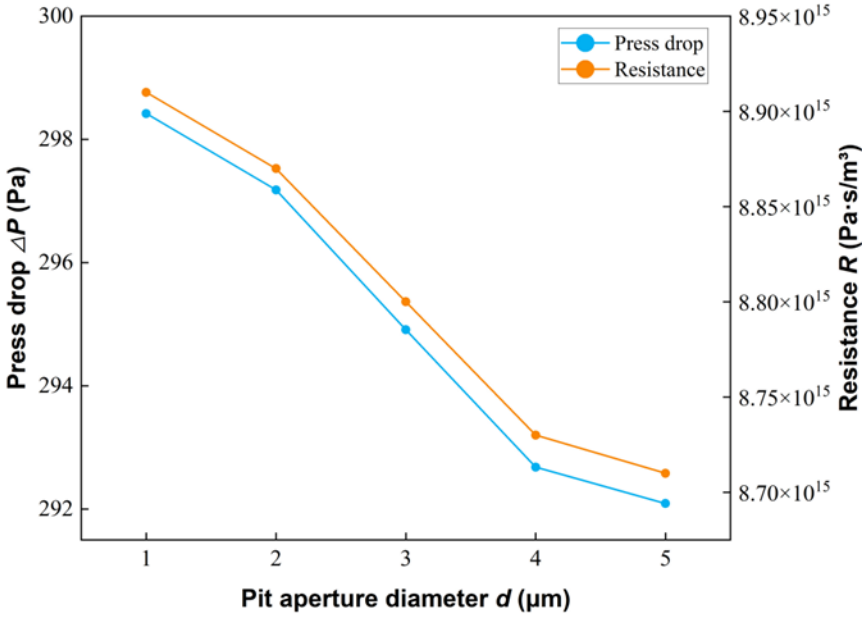


Fig. 4. Effects of pit aperture diameter on press drop and pit flow resistance

Torus Diameter

In comparison to the influence of pit aperture size, an increase in torus diameter exerts a more substantial and nonlinear effect on flow resistance during water transport through pits. As illustrated by the computational results presented in Fig. 5, enlarging the torus diameter from 3.5 to 8.5 μm results in a pronounced rise in the inlet-to-outlet pressure drop, escalating from 280.74 to 796.16 Pa, which corresponds to an increase of 184%. Concurrently, the flow resistance experiences a marked escalation from 8.38×10^{15} to

23.76×10^{15} Pa·s/m³, approaching an order of magnitude increase. It should be noted that the pressure drop approaching 800 Pa in the picture corresponds to an extreme geometric configuration (torus diameter of 8.5 μm within a fixed pit diameter of 10 μm) and is presented for sensitivity analysis rather than to represent a typical physiological condition. Under such high pressure differentials, the rigid margo assumption may become less realistic, as structural deformation could occur and further impede flow. Therefore, these extreme-case results should be interpreted as illustrating the sensitivity of flow resistance to torus size rather than as quantitative predictions of physiological performance. This behavior aligns with observations reported in the physical model developed by Lancashire and Ennos (2002). The primary cause of this significant augmentation in flow resistance is attributed to the reduction of the effectively available flow area within the pit chamber (Qu *et al.* 2021). Specifically, when D remains constant and the torus diameter increases, the effective flow area on the margo surface diminishes, resulting in a substantial increase in the average flow velocity through the margo micropores. This, in turn, induces enhanced viscous dissipation and localized inertial effects within the porous media region.

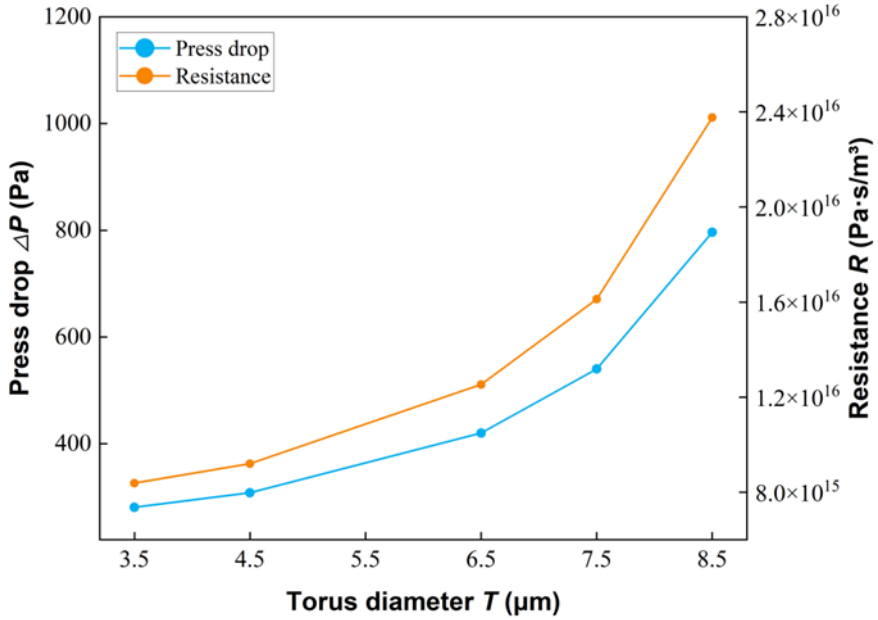


Fig. 5. Effects of torus diameter on press drop and pit flow resistance

Pit Depth

The simulation outcomes demonstrate that an increase in pit depth L exerts a relatively minor influence on the flow resistance within the pit. As illustrated in Fig. 6, when L is increased from 1.8 to 5.8 μm, the pressure drop between the inlet and outlet gradually decreases from 302.25 to 292.26 Pa. Given that the flow rate Q remains constant, the flow resistance correspondingly exhibits only a marginal reduction, declining from 9.02×10^{15} to 8.72×10^{15} Pa·s/m³. Under conditions where other parameters are held constant, an increase in L clearly enlarges the volume of the pit chamber, particularly the region between the margo and the pit border. This enlargement leads to a more gradual velocity gradient before and after the fluid traverses the porous margo region, thereby mitigating local inertial effects. Macroscopically, this phenomenon is reflected in the slight decrease observed in both pressure drop and flow resistance. These simulation results imply that augmenting the L does not fundamentally alter the functional performance of

the pit's core flow structure but rather extends the fluid flow domain within the laminar flow region.

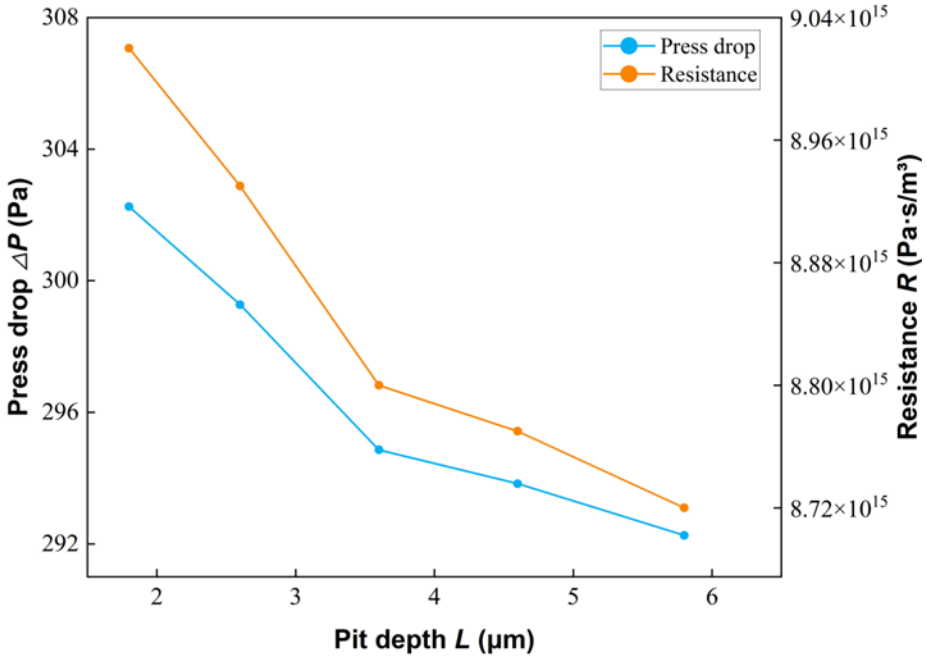


Fig. 6. Effects of pit depth on press drop and pit flow resistance

Margo Thickness

Variations in the thickness *t* of the margo exert a significant regulatory influence on flow resistance. As illustrated in Fig. 7, an increase in thickness from 0.05 to 0.30 μm results in a marked rise in pressure drop, from 110.39 to 622.25 Pa, accompanied by a substantial escalation in flow resistance from 3.29×10^{15} to 18.58×10^{15} Pa·s/m³.

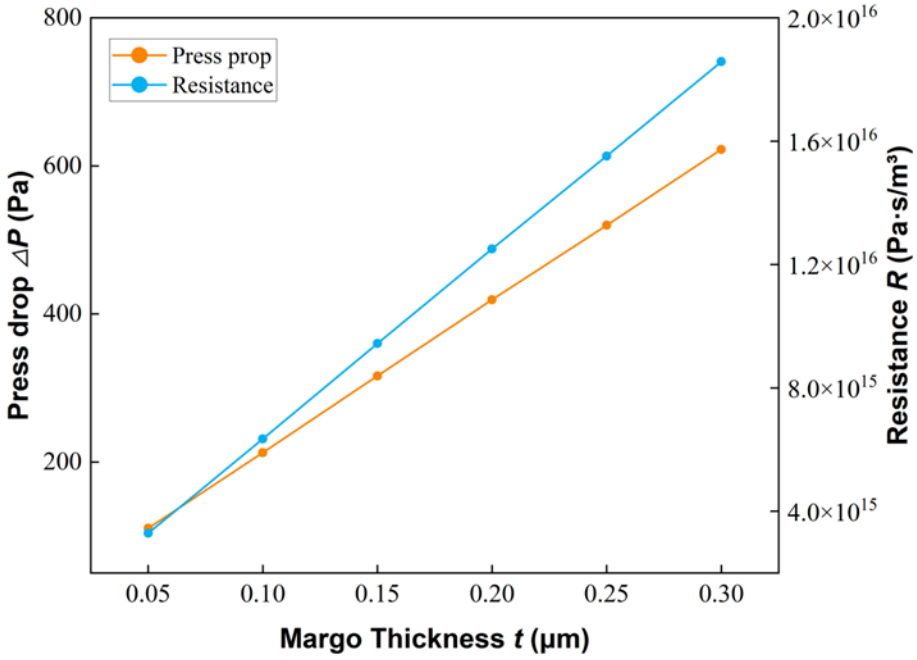


Fig. 7. Effects of margo thickness on press drop and pit flow resistance

From the standpoint of fluid flow dynamics, augmenting the margo thickness effectively lengthens the seepage path and intensifies viscous dissipation within the porous medium. Within the context of the Brinkman equation, even when permeability remains constant, an increase in margo thickness proportionally extends the effective distance over which the Darcy resistance term ($-\mu\vec{u}/\mathrm{K}$) acts, thereby significantly elevating the pressure loss along the flow trajectory. Moreover, analogous to phenomena observed in microchannel flows (Jiang *et al.* 2021; Kristiansen *et al.* 2025; Yang *et al.* 2025), increased thickness amplifies the flow-coupling effects at the interface between the laminar flow region and the porous medium. This leads to heightened velocity gradients and shear stresses in the interfacial zone, which in turn exacerbate local energy dissipation. Collectively, these effects manifest macroscopically as increased pressure drop and flow resistance.

Pit Diameter

Unlike the effects of local parameters such as the pit aperture diameter, variations in the overall pit size exert a more significant and comprehensive influence on flow resistance. As illustrated in Fig. 8, increasing the pit diameter d from 10 to 16 μm results in a reduction of the inlet-to-outlet pressure drop from 300.56 to 266.59 Pa, accompanied by a corresponding decrease in flow resistance from 9.57×10^{15} to 3.32×10^{15} Pa·s/m³.

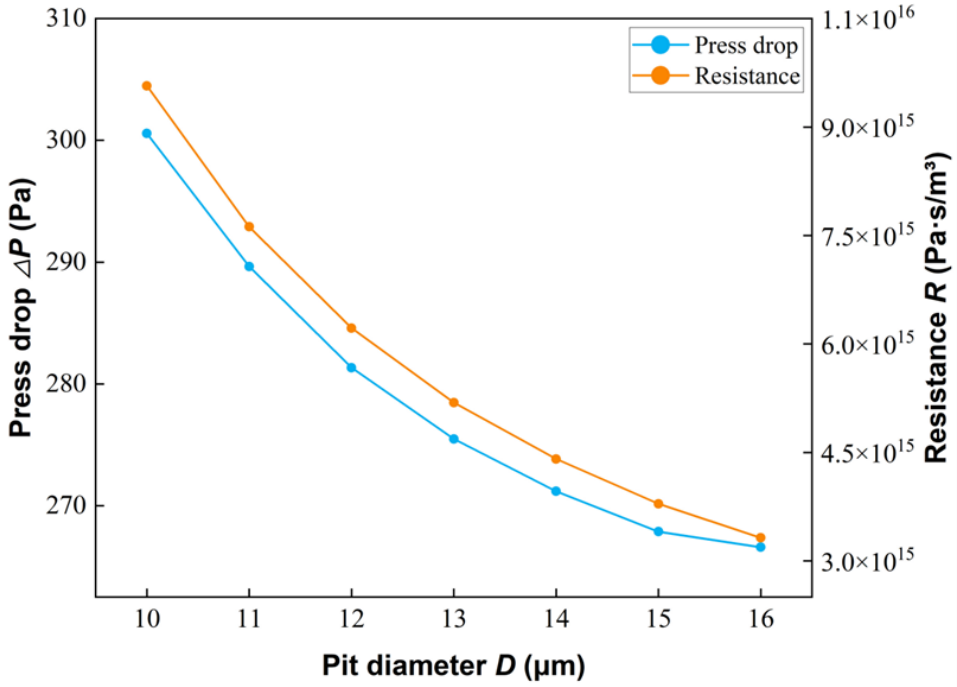


Fig. 8. Effects of pit diameter on press drop and pit flow resistance

Concurrently, as reported in Table 2, the flow within the channel rises from 3.14×10^{-14} to 8.04×10^{-14} m³/s. These changes can be attributed to the multiscale regulatory mechanism associated with the pit diameter D. Specifically, an increase in d directly enlarges the cross-sectional area of the laminar flow region, thereby reducing the local flow velocity, while also substantially expanding the overall area of the margo. Consequently, assuming constant permeability, the enlarged margo area promotes a more gradual velocity distribution within the porous media region, effectively mitigating viscous dissipation and

local pressure losses (Xu *et al.* 2020). Additionally, a larger pit diameter diminishes the velocity gradient at the interface between the laminar and porous media zones, leading to a further reduction in shear stress and the associated flow resistance. Moreover, the increase in pit diameter systematically enhances the fluid storage capacity of the pit chamber, thereby enabling stronger water transport under identical initial pressure conditions (Xia *et al.* 2024). This mechanistic understanding accounts for the observed progressive increase in flow rate Q with increasing pit diameter in the computational results.

Table 2. Hydraulic Transport Capacity Corresponding to Different Pit Diameters

Pit Diameter (μm)	Rate (m^3/s)
10.00	3.14×10^{-14}
11.00	3.79×10^{-14}
13.00	4.52×10^{-14}
14.00	5.31×10^{-14}
15.00	6.15×10^{-14}
16.00	7.06×10^{-14}

Porosity and Micropore Diameter

Figure 9 demonstrates the combined effects of porosity and micropore diameter on the flow resistance within pit structures. According to Eq. 4, the permeability is highly sensitive to changes in porosity and micropore diameter, which leads to significant variations in the flow resistance R with minor adjustments in the flow parameters within the SBD framework, resulting in the nonlinear curve relationship shown in the figure. This sensitivity explains the wide range of flow resistance values observed, from 10^{15} to 10^{17} Pa·s/m³, depending on the specific combination of parameters.

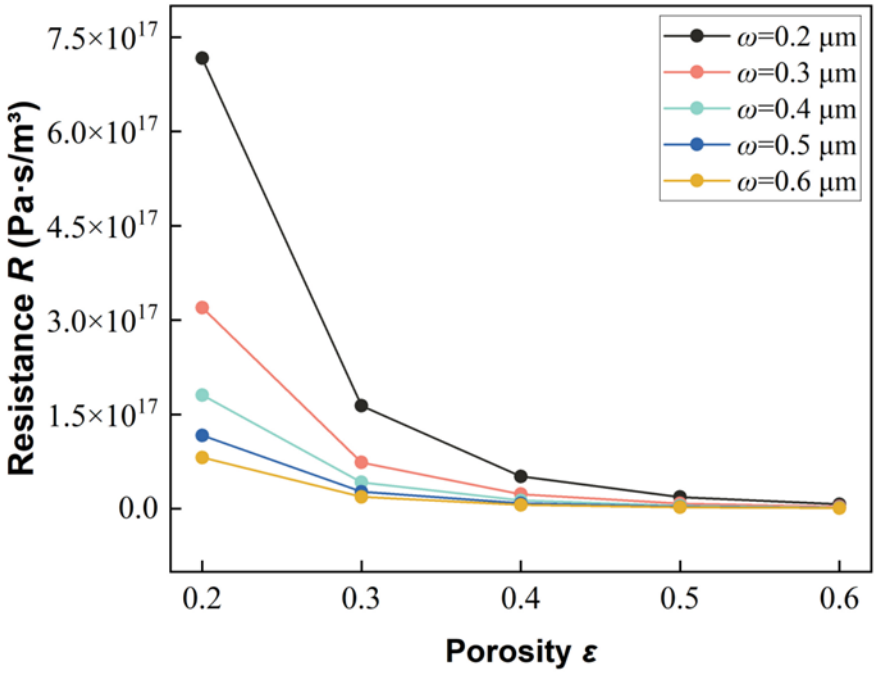


Fig. 9. Effects of porosity and micro-pore diameter on pit flow resistance

When the micropore diameter is held constant, an increase in porosity enlarges the permeable pore space on the margo surface, thereby reducing local flow velocity and pressure loss. This results in a pronounced, nonlinear decrease in the flow resistance of the pit system. For example, considering the curve corresponding to a micropore diameter of 0.2 μm, the permeability is minimal at a porosity of 0.2, resulting in an extremely high flow resistance of 7.17×10^{17} Pa·s/m³. This resistance then rapidly decreases to 1.69×10^{17} Pa·s/m³ at a porosity of 0.3. However, as porosity continues to increase, the rate of decline in flow resistance diminishes; for instance, when porosity rises from 0.5 to 0.6, flow resistance decreases only from 1.17×10^{17} to 0.82×10^{17} Pa·s/m³, a reduction of about 29.9%. This pattern indicates that the regulatory influence of porosity on flow resistance weakens progressively, with the system approaching an asymptotic lower bound of flow resistance.

Conversely, when porosity is fixed and the micropore diameter is increased, pit flow resistance decreases due to enhanced flux through individual micropores. Nevertheless, this effect also exhibits diminishing returns. Notably, once the micropore diameter surpasses 0.2 μm, the rate at which flow resistance decreases with increasing pore diameter slows markedly. Furthermore, the interaction between porosity and micropore diameter becomes saturated in regions of high porosity. As shown in Fig. 9, when the porosity exceeds 0.4, the curves representing the relationship between porosity and flow resistance for different micropore diameters converge and stabilize around 10^{15} Pa·s/m³, corresponding to the baseline parameters of $\varepsilon = 0.44$ and $\omega = 0.2$ μm. These findings suggest that at elevated porosity levels, the margo structure attains an optimal permeability state, whereby further increases in either porosity or micropore diameter confer only marginal improvements in overall hydraulic performance.

CONCLUSIONS

1. The fluid dynamics model of bordered pits based on Stokes-Brinkman-Darcy (SBD) theory, combined with finite element analysis, quantitatively elucidates the influence mechanisms of pit geometry and pore characteristics on the hydraulic efficiency of fluid pathways. This provides an effective analytical tool for revealing the structure–function relationship governing water transport in wood. The model establishes a quantitative map from structural description to functional prediction and confirms the decisive role of margo microstructural features in macroscopic hydraulic conductivity.
2. Simulation results indicate that flow resistance decreases with increasing pit diameter, pit aperture diameter, pit depth, porosity, and micropore diameter, and increases with larger torus diameter and margo thickness. The effects of different structural parameters on flow resistance exhibit a clear hierarchical pattern, with parameters related to the central torus–margo structure exerting the most pronounced influence. This underscores the critical role of the margo as the key component governing water transport in bordered pits.
3. The findings clarify the functional weighting of individual structural parameters in the hydraulic performance of bordered pits and provide quantifiable structural reference thresholds for the optimal design of biomimetic microfluidic devices and advanced wood-based materials. These conclusions are derived directly from parameter sensitivity analysis of the model output and do not involve speculation regarding future research or extended discussion of potential applications.

REFERENCES CITED

Cheng, Z., Guan, H., Meng, J., and Wang, X. (2020). "Dual-functional porous wood filter for simultaneous oil/water separation and organic pollutant removal," *ACS Omega* 5(23), 14096-14103. https://doi.org/10.1021/acsomega.0c01606

Elkady, M. S., Abdelaziz, G. B., Sharshir, S. W., Mohamed, A. Y. A., Elsaid, A. M., El-Said, E. M. S., Mohamed, S. M., Abdelgaied, M., and Kabeel, A. E. (2022). "Non-Darcian immiscible two-phase flow through porous materials (Darcy–Forchheimer–Brinkman model)," *Thermal Science and Engineering Progress* 29, article 101204. https://doi.org/10.1016/j.tsep.2022.101204

Hacke, U. G., and Jansen, S. (2009). "Embolism resistance of three boreal conifer species varies with pit structure," *New Phytologist* 182(3), 675-686. https://doi.org/10.1111/j.1469-8137.2009.02783.x

Held, M., Ganthaler, A., Lintunen, A., Oberhuber, W., and Mayr, S. (2021). "Tracheid and pit dimensions hardly vary in the xylem of *Pinus sylvestris* under contrasting growing conditions," *Frontiers in Plant Science* 12, article 786593. https://doi.org/10.3389/fpls.2021.786593

Igarashi, S., Sasaki, H., and Honda, M. (1988). "Influence of pressure gradient upon boundary layer stability and transition," *Acta Mechanica* 73(1), 187-198. https://doi.org/10.1007/BF01177038

Jiang, X., Xiao, Z., Jiang, J., Yang, X., and Wang, R. (2021). "Effect of element thickness on the pressure drop in the Kenics static mixer," *Chemical Engineering Journal* 424, article 130399. https://doi.org/10.1016/j.cej.2021.130399

Kristiansen, T., Mentzoni, F., and Molin, B. (2025). "The role of plate-end separation and plate thickness of perforated plates in oscillatory flow," *Physics of Fluids* 37(9), article 0278480. https://doi.org/10.1063/5.0278480

Lancashire, J. R., and Ennos, A. R. (2002). "Modelling the hydrodynamic resistance of bordered pits," *Journal of Experimental Botany* 53(373), 1485-1493. https://doi.org/10.1093/jexbot/53.373.1485

Lesinigo, M., D'Angelo, C., and Quarteroni, A. (2010). "A multiscale Darcy–Brinkman model for fluid flow in fractured porous media," *Numerische Mathematik* 117(4), 717-752. https://doi.org/10.1007/s00211-010-0343-2

Li, S., Wang, J., Yin, Y., Li, X., Deng, L., Jiang, X., Chen, Z., and Li, Y. (2020). "Investigating effects of bordered pit membrane morphology and properties on plant xylem hydraulic functions—A case study from 3D reconstruction and microflow modelling of pit membranes in angiosperm xylem," *Plants* 9(2), article 231. https://doi.org/10.3390/plants9020231

Parent, L. R., Bakalis, E., Proetto, M., Li, Y., Park, C., Zerbetto, F., and Gianneschi, N. C. (2018). "Tackling the challenges of dynamic experiments using liquid-cell transmission electron microscopy," *Accounts of Chemical Research* 51(1), 3-11. https://doi.org/10.1021/acs.accounts.7b00331

Qu, W., Yang, C., Ma, Y., Yu, W., Qin, G., and Jin, Y. (2021). "Analysis of the structure and hydraulic function of bordered pits using the lattice Boltzmann method," *Forests* 12(5), article 526. https://doi.org/10.3390/f12050526

Ruan, L., and Rybak, I. (2025). "A hybrid-dimensional Stokes–Brinkman–Darcy model for arbitrary flows to the fluid–porous interface," *Transport in Porous Media* 152(10). https://doi.org/10.1007/s11242-025-02220-1

Ruan, L., and Rybak, I. (2026). "Stokes-Brinkman-Darcy models for fluid-porous

systems: Derivation, analysis and validation," *Applied Mathematics and Computation* 510, article 129687. https://doi.org/10.1016/j.amc.2025.129687

Schulte, P. J. (2011). "Computational fluid dynamics models of conifer bordered pits show how pit structure affects flow," *New Phytologist* 193(3), 721-729. https://doi.org/10.1111/j.1469-8137.2011.03986.x

Schulte, P. J., Hacke, U. G., and Schoonmaker, A. L. (2015). "Pit membrane structure is highly variable and accounts for a major resistance to water flow through tracheid pits in stems and roots of two boreal conifer species," *New Phytologist* 208(1), 102-113. https://doi.org/10.1111/nph.13437

Tripathi, V. K., Raju, C. S. K., and Yook, S.-J. (2025). "Stability analysis of bidispersive porous convection with maximum density and variable viscosity effects," *Physics of Fluids* 37(2). https://doi.org/10.1063/5.0254005

Xia, P., Wu, Y., Song, W., Xie, L., Jia, Z., Wang, X., and Li, Q. (2024). "The fluid–solid interaction in the nonlinear pressure–flux relationship of bordered pits in oriental arborvitae (*Platycladus orientalis*)," *Forests* 15(1), article 181. https://doi.org/10.3390/f15010181

Xu, T., Zhang, L., and Li, Z. (2020). "Computational fluid dynamics model and flow resistance characteristics of *Jatropha curcas* L xylem vessel," *Scientific Reports* 10(1), article 14728. https://doi.org/10.1038/s41598-020-71576-9

Yang, L., Zhang, X., Yan, Y., Wu, L., Zheng, C., Wang, B., Cui, Z., Shao, C., and Cheng, L. (2025). "Transition from non-uniform to smooth ^{4}He flow in micro-orifices: The impact of thickness on pressure drop and entropy production," *Physics of Fluids* 37(8), article 0283725. https://doi.org/10.1063/5.0283725

Article submitted: February 19, 2026; Peer review completed: March 8, 2026; Revised version received: March 12, 2026; Accepted: April 12, 2026; Published: May 18, 2026.
DOI: 10.15376/biores.21.3.5984-5998